Manipulating Photoadsorption Kinetics: NO on Cl-Treated Fe$_2$O$_3$

E. R. Blomiley and E. G. Seebauer*

Department of Chemical Engineering, University of Illinois, Urbana, Illinois 61801

Received: December 30, 1998; In Final Form: April 12, 1999

While chemical surface modification is commonly employed to improve the performance of solid catalysts, this approach has been largely neglected in optimizing photoadsorbents. Here we show that powdered Fe$_2$O$_3$ treated with aqueous NH$_4$Cl and subsequently calcined near 300 °C exhibits appreciable activity for the photoadsorption of NO, whereas the pure iron oxide does not. We employ a uniquely configured reactor to develop well-characterized photoadsorption kinetics without shadowing or diffusion effects. Kinetics obey simple Langmuir-type expressions for nondissociative adsorption. However, the adsorption process requires the simultaneous presence of adsorbed chlorine and H$_2$O, and X-ray photoelectron spectroscopy shows that both the +2 and +3 oxidation states of iron play a role. This complexity mirrors corresponding complexity in the bonding of NO to Fe cations in the analogous aqueous-phase coordination chemistry. Interestingly, the photoadsorbent is not poisoned by exposure to SO$_2$ or CO$_2$.

Introduction

Photostimulated catalysis on semiconductor surfaces offers an attractive tool for applications in environmental cleanup and pollution prevention. Despite intensive effort, however, several fundamental aspects of the catalytic process remain poorly explained.[1−5] Typically, catalysis involves adsorption, surface diffusion, surface reaction, and desorption; in principle, illumination can affect any or all of these steps. Indeed, photon influences on adsorption,[6−8] surface diffusion,[9] and desorption[6,10,11] have been unambiguously identified. However, since the component steps in isolation typically have less practical application than photocatalysis, they have attracted less attention.

In this paper, we examine such a component step: photoadsorption. In particular, NO photoadsorption on Fe$_2$O$_3$ serves not only to elucidate larger issues in photocatalysis but also to offer significant potential applications in its own right. Large amounts of NO appear in flue gas streams from high-temperature combustors. This NO participates in the generation of many other noxious or acidic atmospheric species, making removal imperative. Some workers have examined photoadsorption on inexpensive semiconducting metal oxides, such as Fe$_2$O$_3$, TiO$_2$, and ZnO,[12−15] as an alternative to the expense of conventional selective catalytic reduction. Adsorption rates on the untreated materials fall far below those needed for practical applications, however. Attempts at improvement have focused primarily on adding dopants,[16,17] with a view toward increasing the usable portion of the illuminating light's spectrum [18,19] or inhibiting the recombination of electron hole pairs.[20,21]

We take another approach in the present work. Rather than manipulating bulk properties, we influence the adsorption process by treating only the surface (as is often done in catalysis). Previous studies have suggested a dependence of photoadsorption rate on surface composition. For example, oxygen photoadsorption rates on TiO$_2$ depend on the heating history.[22−25] We employ a much more forceful approach for rate enhancement by introducing new chemical elements to the photoadsorbent surface. The present work focuses on uptake measurements; related work probes the nature of the photoadsorbed

species via temperature programmed desorption.[26] To reproduce the form of the adsorbent as it might be used in actual applications, we examine the material in powder form. This approach presents unique challenges for quantitative rate measurement, including the creation and characterization of a well-defined illumination geometry and the avoidance of intra- and interparticle diffusion effects. Hence, this paper describes the experimental methods in detail.

Experiment

Experiments were performed in a custom-built anodized aluminum photoreactor with a volume of 0.5 l. Figure 1 shows a schematic diagram. A mechanical vacuum pump evacuated the reactor during flow experiments, and was capable of maintaining a base pressure near 15 mTorr. A capacitance manometer monitored pressure continuously. Precision needle valves independently throttled each gas into a manifold for thorough mixing prior to entrance into the reactor. A differentially pumped quadrupole mass spectrometer monitored gas composition up to 5 masses simultaneously. The differential pumping scheme employed an ion pump together with a series of throttling valves controlling flow through $^1/_4$ in. stainless steel tubing. The pressure in the sampling chamber remained below 5×10^{-7} Torr at all times. Calibration experiments in which we raised the reactor pressure in stepwise fashion showed negligible delays in the gas sampling arrangement.

The reactor body and sample mount were designed specifically for well-characterized photoillumination of fine powders. An unfocused 100 W Hg arc lamp illuminated the adsorbents through a 13 cm diameter Pyrex window. We extensively characterized the spectral and spatial properties of the illuminating beam with a small-area photodiode. Over the 50 cm^2 area typically occupied by an adsorbent, the unfiltered beam flux remained constant to within 10% at 3.2×10^{17} photon/cm^2 s ($300 < \lambda < 600$ nm). Below 300 nm, lamp output combined with dramatically decreased transmission through Pyrex cut the incident photon flux to negligible levels. Above 600 nm, Fe$_2$O$_3$ no longer absorbed light (and as will be shown, the photoactivity dropped to zero). We also characterized the spectral distribution of the incident light with a monochromator together with a

---
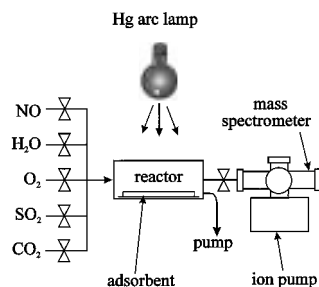
Figure 1. Schematic drawing of the apparatus.

TABLE 1: Materials and Treatments

treatment	materials	photoactivity
no treatment	pure oxides of iron, titanium	inactive
	flyash	inactive
	$Fe_2O_3 + TiO_2$ (15−85%)	inactive
chlorine treatment	$Fe_2O_3 + NH_4Cl$	active
	$FeCl_3 + NH_4OH$	active
	$Fe_2O_3 + Cl_2(g), HCl(g), HCl(aq)$	inactive
	TiO_2, flyash + NH_4Cl	inactive
other halide	$Fe_2O_3 + NH_4Br, NH_4F$	inactive
	$Fe_2O_3 + HBr(g) + HF(g)$	inactive
	$TiO_2 + NH_4Br, NH_4F$	inactive
other impregnations	$Fe_2O_3, TiO_2 + NaOH$	inactive
	$Fe_2O_3, TiO_2 + KOH$	inactive
	$Fe_2O_3, TiO_2 + Ca(OH)_2$	inactive

calibrated photodiode. The broadband radiation exhibited sharp peaks at the Hg emission lines near 365, 436, 546, and 577 nm. Some adsorption experiments required controlled attenuation of the broadband light. Fused-silica neutral-density filters having optical densities between 0.03 and 1.0 served this purpose. Other experiments focusing on spectral dependence of adsorption rate demanded essentially monochromatic illumination. A set of colored glass band-pass filters accomplished this purpose, each having a passwidth of 10 nm. Photon fluxes through each filter were measured with a calibrated photodiode.

The adsorbent rested in a very thin layer upon a sheet of filter "paper" made of glass fiber. This configuration held the adsorbent in place during flow experiments while minimizing particle shadowing. Optical microscopy confirmed less than 10% shadowing. The particle separation also minimized interparticle diffusion limitations. Because the particles were not porous, there was no concern about intraparticle diffusion. A typical experiment employed about 40 mg of solid.

The principal photoadsorbent material we studied was prepared by mixing 50 g powdered α-Fe_2O_3 (Fisher Chemical) with an aqueous solution of 54 g NH_4Cl (Fisher Chemical). After evaporation of the water, the remaining dry solid was crushed to a powder and calcined in slowly flowing N_2 at 300 °C for 8 h unless otherwise stated. To crudely characterize water-soluble species desorbing from the solid during calcination, the effluent gas was bubbled through 50 mL of distilled H_2O. The material was crushed again and sieved to remove particles larger than 100 μm before storage in airtight containers. The average particle size was 2 μm, with a fairly wide distribution. We estimate the solid to have an area of about 1 m^2/g. Washing the material with water either before or after calcination resulted in complete loss of photoactivity.

We also prepared many other materials as detailed in Table 1. Besides the adsorbent described above, only one other solid displayed significant photoactivity. This material was produced by precipitating iron oxy-hydroxide by adding aqueous NH_4OH to a solution of $FeCl_3$. The resulting solid was dried (without washing) and calcined as described above. While this adsorbent displayed activity comparable to that of the treated
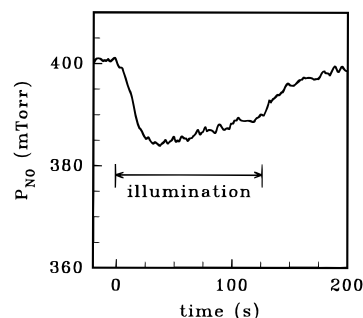

Figure 2. Typical temporal profile of the NO pressure in the reactor during photoadsorption. This particular case describes room-temperature adsorption for Fe_2O_3 treated with NH_4Cl and calcined to 300 °C. Unless stated otherwise, succeeding figures also employ data from this material.

Fe_2O_3, the photoadsorption rates depended sensitively on the details of the preparation process. We believe that the two adsorbents exhibit roughly similar surface compositions and adsorption chemistries, but that treating Fe_2O_3 represents a more controllable preparation procedure. Hence, we focused our efforts on this approach.

After charging with fresh adsorbent, the reactor was evacuated for five minutes down to its base pressure. The gas mixture was then admitted absent illumination for two minutes to stabilize the flow and gas composition. We took care to reproduce these procedures carefully, because variations caused irreproducibilities associated with exposure to H_2O as described in the Results. Upon illumination, photoadsorption took place under continuous flow conditions with gas residence times near 25 s. We consider the reactor to be well-mixed under these conditions. Typically adsorption removed about 5% of the NO. Control experiments showed that no measurable adsorption took place in the absence of either adsorbent or illumination. As expected, total adsorption rates scaled linearly in the mass of solid charge. After adsorbing for 5−600 s, we blocked the light source. Then we stopped the gas flow abruptly to measure precisely the gas residence time (needed for quantitative adsorption rate calculation).

We attempted to simulate real flue gas conditions as much as possible. For example, we employed 400 mTorr of NO unless otherwise stated. In a few experiments probing the robustness of adsorption to contamination, we added 750 mTorr CO_2 and 500 mTorr SO_2. All these pressures equal those typically present in a combustion flue. However, the need for well-mixed flow and controllable gas sampling for mass spectroscopy limited the maximum possible pressure in our setup to a few Torr. Thus, we eliminated all N_2 (considered inert here) and reduced the pressures of other flue gas components to 400 mTorr O_2 and 300 mTorr H_2O unless otherwise stated. All gases were reagent grade, used without further purification. Water originated from a bubbler containing deionized H_2O. Unless otherwise stated, adsorption always took place at room temperature (25 °C). However, some experiments were performed at 100 °C by wrapping electrical heating tape around the reactor.

For some adsorbents we analyzed surface composition and chemical state with X-ray Photoelectron Spectroscopy (XPS) using a Mg Kα anode at 400 W. Composition calculations employed manufacturer-determined elemental sensitivities. The adventitious carbon peak at 285 eV served to calibrate energies.

Results

Figure 2 shows the temporal evolution of NO pressure during a typical adsorption experiment. Upon broadband illumination,

Manipulating Photoadsorption Kinetics

J. Phys. Chem. B, Vol. 103, No. 24, 1999 **5037**
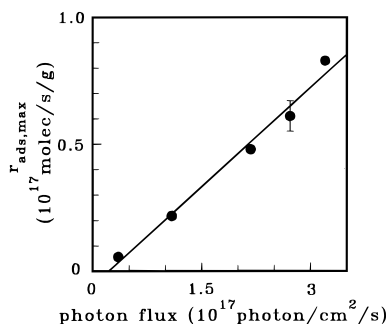
Figure 3. Dependence of the maximum adsorption rate $r_{ads,max}$ on broadband illumination intensity. Behavior is linear.
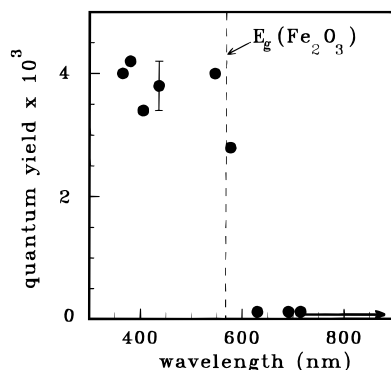
Figure 4. Spectral dependence of the quantum yield for photoadsorption of NO. The arrow originating from the point at 715 nm signifies use of a redpass filter instead of a band-pass filter as with the other points. The dashed vertical line shows the band gap energy E_g for α-Fe_2O_3 (2.2 eV, 565 nm).

the NO pressure dropped rapidly to a minimum (though not instantaneously because of reactor residence time effects). After reaching this minimum, the NO pressure then began to increase slowly. We attribute this increase to progressive site filling, consistent with other results we have obtained using temperature programmed desorption (TPD).[26] Interestingly, small amounts of H_2O desorbed during NO adsorption. The H_2O pressure increase constituted about 10% of the NO pressure decrease. Upon cessation of illumination, NO pressure recovered back to its original base line with a time constant near the gas residence time.

The minimum in NO pressure shown in Figure 2 signifies a maximum $r_{ads,max}$ in the adsorption rate r_{ads}. Figure 3 shows that $r_{ads,max}$ scaled linearly in photon flux. Figure 4 shows the spectral dependence of the adsorption rate. Since $r_{ads,max}$ varies with photon flux, and the flux varied greatly through our band-pass filters (due to variations in both source brightness and filter transmissivity), we have plotted photoactivity in the form of a quantum yield. We define this yield as the rate of NO adsorption per unit area of directly illuminated solid (molec/cm² s) divided by the incident photon flux (photons/cm² s). We estimated the directly illuminated solid area by assuming that only half of the total specific surface area of 1 m²/g was active. This estimate neglects backreflection from the glass fiber substrate onto the undersides of the particles and also ignores differences in local intensity due to the spherical shape of the particles (meaning oblique illumination over most of a particle surface). The quantum yield remains essentially constant at 4×10^{-3} below about 550 nm, but then decreases sharply to zero above about 630 nm. For comparison, the band gap energy E_g of 2.2 eV for Fe_2O_3[27−29] also appears in Figure 5, falling at 565 nm. The sharp decrease clearly coincides with E_g, as expected for the photoresponse of a semiconductor.
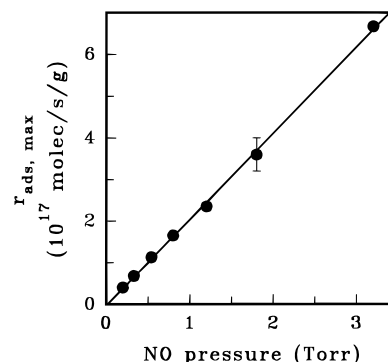
Figure 5. Dependence of the maximum adsorption rate $r_{ads,max}$ on NO pressure initially admitted to the reactor. Behavior is linear.

Figure 5 shows $r_{ads,max}$ as a function of NO pressure during photoadsorption; first order behavior is readily apparent. Uptake data like those of Figure 1 provide the additional information needed to determine the sticking probability S and its dependence on coverage θ. This experiment represents a form of the technique described by King and Wells[30] for work with molecular beams in ultrahigh vacuum. A mass balance on NO in the gas-phase yields the following equation for the pressure P of NO as a function of time t:

$$\frac{dP}{dt} = \frac{P_o - P}{\tau} - \frac{Wr_{ads}RT_g}{V} \tag{1}$$

where P_o denotes the pressure prior to photoadsorption, τ the reactor residence time, V the reactor volume, T_g the gas temperature, R the universal gas constant, and W the mass of solid. In this equation, the instantaneous adsorption rate r_{ads} takes on mass-normalized units, molecule/gs, and is given by

$$r_{ads} = S(\theta)P/A_s(2\pi MkT_g)^{1/2} \tag{2}$$

where A_s denotes the specific surface area of the solid, $S(\theta)$ the coverage dependent sticking probability, M the molecular mass, and k Boltzmann's constant. The initial condition for the differential equation given by eqs 1 and 2 is

$$P(0) = P_o \tag{3}$$

Since this differential equation contains θ, we must write a separate mass balance for this quantity. Ordinarily θ is defined by the areal adsorbate density n (in molec/cm²), and is often referenced to the saturation density n_{sat}. However, θ can also be defined by mass-based adsorbate density N (in molec/g) and referenced to a corresponding saturation density N_{sat}. Thus,

$$\theta = n/n_{sat} = N/N_{sat} \tag{4}$$

For this analysis it proves convenient to work with the mass-normalized density. Thus, the mass balance for θ becomes:

$$d\theta/dt = r_{ads}/N_{sat} \tag{5}$$

with initial condition:

$$\theta(0) = 0 \tag{6}$$

Equations 1 and 5 form a system of two ordinary differential equations that in general must be solved numerically. Under conditions of very fast pumping, the eigenvalues become widely separated, with one corresponding to τ and the other to the effective time constant for adsorption. In this case, dP/dt

5038 *J. Phys. Chem. B, Vol. 103, No. 24, 1999*

Blomiley and Seebauer
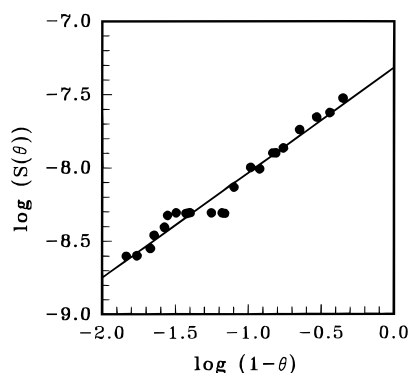
Figure 6. Dependence of the sticking probability $S(\theta)$ on unoccupied site density $(1-\theta)$. $S(\theta)$ here is computed in the fast-pumping approximation according to eq 10.

Figure 7. Numerical solution of eqs 1 and 5 used to obtain S_o, assuming $m = 1$.

Figure 8. Dependence of $r_{ads,max}$ on H_2O pressure, showing nonmonotonic behavior.

becomes very small compared to $(P_o - P)/\tau$, and r_{ads} (and therefore S) becomes proportional to the instantaneous change in system pressure. Unfortunately, very fast pumping usually corresponds to very small signals $P_o - P$. To make the pressure change observable, we had to increase τ to 25s, which in our case had the effect of moving the eigenvalues much closer to each other. Thus, the fast-pumping approximation could be employed only to first order. More accurate determination of the parameters required the following bootstrap procedure.

We first parametrized S according to the standard form drawn from Langmuir adsorption kinetics:

$$S(\theta) = S_o(1 - \theta)^m \qquad (7)$$

Since any deviation of P from P_o could be directly attributed to adsorption, the saturation densities N and N_{sat} needed for θ could be determined by direct temporal integration of the pressure—time data.

$$N = \int_o^t \frac{(P_o - P(t'))V}{RT_g}dt' \qquad (8)$$

and

$$N_{sat} = \int_o^\infty \frac{(P_o - P(t'))V}{RT_g}dt' \qquad (9)$$

This procedure yielded $N_{sat} = 9.5 \times 10^{18}$ molecule/g. With our visual estimate for the illuminated surface area, this number translates into an areal density of $n_{sat} = 1 \times 10^{15}$ molecule/cm^2, or about 1 monolayer assuming a van der Waals packing radius of 2 Å.[31]

The fast pumping approximation becomes increasingly accurate as the surface saturates, and the instantaneous time constant for adsorption becomes small as adsorption slows. In this case, dP/dt becomes small compared to $(P_o - P)\tau$, and eqs 1 and 2 combine to yield the algebraic equation

$$S = S_o(1-\theta)^m = \sqrt{2\pi MkT_g}\frac{A_s}{A}\frac{V}{PRT_g}\frac{P_o - P}{\tau} \qquad (10)$$

Taking the logarithm of both sides and using eq 7 indicates that a plot of $\log(S)$ vs $\log(1-\theta)$ should yield a line of slope m. Figure 6 shows such a plot for $\theta > 0.5$. The slope gives $m = 0.8$ with an uncertainty due to a random error of 0.1. Given the systematic uncertainty entailed by employing the fast-pumping approximation, and independent TPD data showing $m = 1.0 \pm$
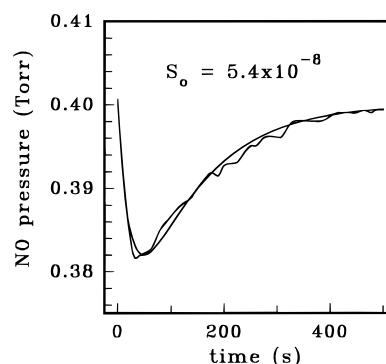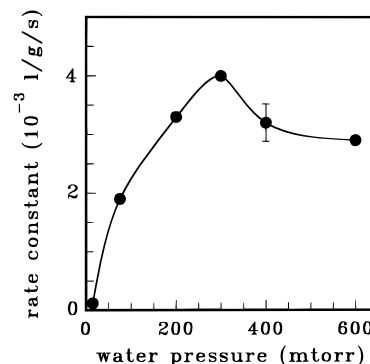
0.1 for states desorbing below 157 °C,[26] we believe our present data are most consistent with a value of $m = 1$.

While the previous step formally yields a value for S_o, a more accurate number comes from a direct fit of data for $P(t)$ using S_o as the single-variable parameter. Figure 7 shows such a fit obtained by numerically solving the coupled differential equations 1 and 5 using $m = 1$. A nonlinear least-squares fit to the data yielded $S_o = 5.4 \times 10^{-8}$. Note that the fit is quite good, confirming the previously calculated valued for m and N_{sat}.[32]

Variations in O_2 pressure in a range from 50 to 800 mTorr exerted no effect on $r_{ads,max}$. H_2O presented a complex picture, as shown in Figure 8. No NO photoadsorbed below 20 mTorr of H_2O. However, at higher pressures, $r_{ads,max}$ increased to a maximum at 300 mTorr H_2O before decreasing again. Interestingly, $r_{ads,max}$ depended not only on the H_2O pressure during illumination but also on the history of exposure to H_2O prior to photoadsorption. Increased exposure generally led to increased values of $r_{ads,max}$.

Photoadsorbent activity remained unaffected by short-time exposure to potential gas poisons and to modestly elevated temperatures. Figure 8 shows $r_{ads,max}$ in the presence and absence of SO_2 and CO_2. Both gases often poison catalysts.[33,34] However, Figure 9 shows that these gases have no measurable effect on $r_{ads,max}$. In addition, we monitored the SO_2 and CO_2 instantaneous pressures for signs of adsorption, but found none. Figure 10 compares $r_{ads,max}$ measured at 25 and 100 °C, since photoactivity at modestly elevated temperatures is a necessity for flue gas applications. No effect of temperature on activity appears in Figure 10.

Calcination temperature proved to be an important factor in photoadsorbent activity. Figure 11 shows the properties of NH_4Cl-treated solids calcined at temperatures ranging from 150 to 400 °C for 8 h. Only temperatures between 250 and 350 °C yielded material with significant photoactivity; 300 °C yielded

Manipulating Photoadsorption Kinetics

J. Phys. Chem. B, Vol. 103, No. 24, 1999 **5039**
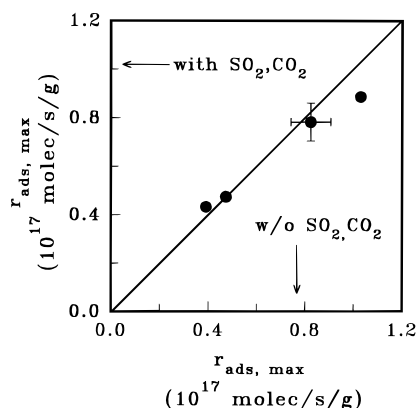
Figure 9. Maximum adsorption rate $r_{ads,max}$ in the presence of 500 mTorr SO_2 and 750 mTorr CO_2 plotted against $r_{ads,max}$ without these gases. Adsorption rate of NO is remains unaffected.
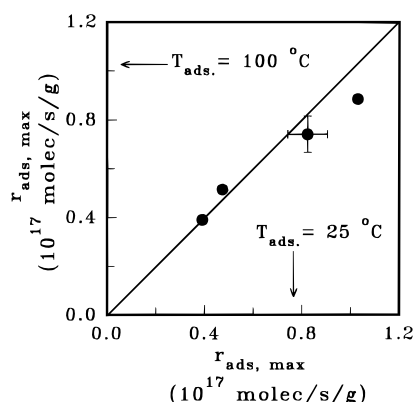

Figure 10. Maximum adsorption rate $r_{ads,max}$ at 100 °C vs $r_{ads,max}$ at 25 °C. Adsorption rate of NO is unaffected by temperature in this range.
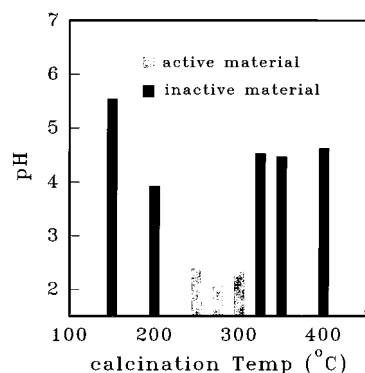
Figure 11. Dependence of adsorbent acidity on calcination temperature.

the highest rates. Figure 11 also shows the results of a crude acidity test we applied to each material. We gauged acidity by stirring 4 g of photoadsorbent in 1 L of deionized H_2O and measuring the pH of the solution. This pH appears in Figure 11, and exhibits the lowest levels for the most active adsorbents. To further characterize this effect, we measured the pH of the water through which the gaseous effluent from calcination was passed. The pH of these solutions was always basic, and varied inversely with the acidity of the remaining solid recorded in Figure 11. For the most active material at 300 °C, the pH of the effluent-treated water reached 12.

These observations imply changes in surface composition with calcination temperature, which we confirmed with XPS. Figure 12 displays a resulting wide spectrum scan of fresh adsorbent calcined at 300 °C. The following species appear: Fe $(2p_{3/2})$ at
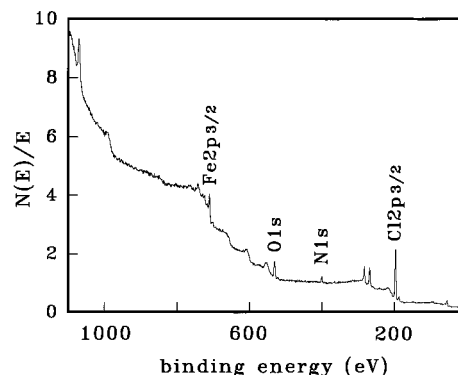
Figure 12. Wide-spectrum XPS of the active photoadsorbent.

TABLE 2: XPS Compositions

history	calcination T (°C)	% Fe	% O	% Cl	% N
fresh photoadsorbent	150	25	28	32	15
	300	21	21	47	11
	325	39	58	1	2
	350	37	61	2	0
	400	37	61	2	0
after NO adsorption	300	22	22	47	9
after NO desorption	300	24	23	42	11

712 eV, O (1s) at 530 eV, N (1s) at 402 eV, and Cl $(2p_{3/2})$ at 199 eV. Table 2 shows corresponding atomic composition of this material together with others calcined at temperatures ranging from 150 to 400 °C. Nitrogen begins to disappear significantly above 150 °C. Both chlorine as well as nitrogen essentially vanish above 300 °C.

Table 2 also presents atomic compositions of adsorbent calcined at 300 °C and thereafter subjected to NO photoadsorption. In these experiments, the glass-fiber substrate was replaced with a thin silicon wafer coated with native oxide. This arrangement permitted rapid sample heating and cooling without corresponding heating of the reactor. Reference 26 describes the modified configuration in detail. In one experiment, we conducted XPS a few minutes after NO photoadsorption to saturation. The adsorbent was exposed to air in the period intervening between adsorption and analysis. In another experiment, we repeated the procedure except for heating the adsorbent to 157 °C in the dark for 45 s immediately after photoadsorption. This temperature corresponds to the maximum at which TPD spectra exhibit perfectly reversible photoadsorption[26] and show desorption of about 10% of the NO. The compositions in Table 2 show no significant change for any species when proceeding from the fresh surface through photoadsorption to partial desorption. While the data for Cl are consistent with a slight decrease in the desorption step, the change is too small given the experimental uncertainties to accept with confidence.

The more interesting results provided by XPS in this adsorption sequence concern the oxidation state of the iron. On the unadsorbed surface, we positively identified the $2p_{3/2}$ peak of Fe^{2+} at 711 eV and of Fe^{3+} at 713 eV. We also detected corresponding peaks at the weaker $2p_{1/2}$ transition at 724 and 726 eV for Fe^{2+} and Fe^{3+}, respectively. We employed manufacturer-supplied software for spectral deconvolution and peak area calculation. Fresh photoadsorbent with no prior exposure to NO showed about 10% of the total iron as Fe^{2+}, with the balance as Fe^{3+}. However, photoadsorption converted all of the iron into the +3 state. Finally, partial desorption of NO yielded the original composition, with about 10% Fe^{2+}.

Blomiley and Seebauer

Discussion

As shown in Figure 3, the photoadsorption rate varies linearly with photon flux. This behavior in photoadsorption accords well with observations in photocatalysis at modest illumination intensities.[35–39] At higher intensities, roughly 2 orders of magnitude above those used here, photocatalytic rates become sublinear, scaling with the square root of the illumination intensity.[35,36] This effect has previously been attributed to photon-induced band flattening.[35,38,39] We are not aware of measurements concerning the intensity dependence of adsorption rates. However, our data suggest that the governing physics in photoadsorption and photocatalysis are similar. Explanations for the effect on catalytic degradation rates generally focus on increased recombination rates of the photogenerated electron–hole pairs.[35,38,39]

The spectral dependence of photoactivity shown in Figure 4 shows the classic cutoff at the bulk energy gap of the semiconductor substrate. We observed cutoff near the quoted value of E_g for α-Fe_2O_3 (2.2 eV at 25 °C).[27–29] While our value for E_g is not especially precise, clearly we have not affected E_g significantly. Some workers have added dopants to bulk semiconductors in an attempt to decrease E_g and thereby employ a large fraction of the incident broadband radiation[18,19] Clearly our surface treatment does not function this way. The disappearance of photoactivity for our solids upon simple washing confirms the notion that we have not introduced bulk dopants. In any case, our preparation and calcination took place at 300 °C, which is a small fraction of the Fe_2O_3 melting point of 1565 °C. Thus, little diffusion into the bulk should have occurred.

Figures 4 and 6 indicate standard Langmuir-type adsorption kinetics for NO that are first order in empty site density. These results accord well with those we have obtained independently by temperature programmed desorption (TPD) in this system.[26] NO also exhibited molecular desorption in TPD with first-order kinetics. Taken together, the results suggest simple nondissociative adsorption.[40]

Closer examination of the data reveals more complex features to the adsorption, however. For example, the simultaneous presence of water, chlorine and light prove necessary to the adsorption process.[41] Water often plays a mediating role in photostimulated reaction[42,43] and adsorption[6,8,13,23,25] on metal oxide surfaces. In reaction, adsorbed water provides hydroxyl ions, which photogenerated charge carriers convert into active hydroxyl radicals that drive further reaction steps directly. This mechanism explains water-enhanced rates in photooxidation of oxygenated organic species, for example.[42,43]

The effects of H_2O on photoadsorption remain less well-understood, probably because most work has focused on a single adsorption system: O_2 on TiO_2. In that case, photooxidation of adsorbed hydroxyl ions is also invoked to explain water-enhanced photoadsorption, although the postulated mechanism differs.[6,8,23,25] Undoped TiO_2 functions naturally as an n-type semiconductor. Illumination therefore generates a large fractional increase in hole concentration, which facilitates the conversion of hydroxyl ions to radicals:

$$OH^- + p^+ \longrightarrow \bullet OH(ad) \qquad (11)$$

However, the radicals do not facilitate photoadsorption directly. Instead, the ions are hypothesized to serve as a sink for holes, thereby leaving excess photoelectrons available to convert O_2 into a stably adsorbed O_2^- species. A similar mechanism has been invoked to explain the (relatively slow) rate of NO photoadsorption on TiO_2.[13] In this case, the adsorbate converts into NO^- or NO_2^-.

The temperature invariance of photoactivity observed here is consistent with this picture, since hydroxyl groups remain adsorbed on transition metal oxides up to 300 °C or more.[6] Interestingly, we found that increasing the water pressure above 300 mTorr resulted in a slight decrease in adsorption rate. We observed a similar effect in TPD.[26] As with photoreaction,[43] we suspect that excessive water simply blocks active sites for NO adsorption.

Unfortunately, this picture implicitly draws upon many assumptions that may not be valid. For example, neither the direction nor the magnitude of band bending is known for the powders we used, either in the dark or under illumination. The electric fields created by such bending could easily drive the adsorption-enhancing photoelectrons away from the surface. Furthermore, for this mechanism to operate over substantial periods of time, ions must somehow reappear after the photogeneration of radicals. Nothing is said about how such a process operates. Unfortunately, the overall question of water-enhanced photoadsorption cannot be resolved with the current state of knowledge of metal oxide surfaces. Indeed, many of the required physical parameters remain poorly characterized even for heavily studied semiconductors such as silicon.[44]

The role of Cl presents a puzzle even more difficult than that of water. Not just any form of chlorine will do: exposure of Fe_2O_3 to HCl (either gaseous or aqueous) or Cl_2 do not yield an active adsorbent. The NH_4Cl-treated solids display no activity before calcination, either. Furthermore, use of NH_4F or NH_4Br does not enhance activity. In other words, the activity of calcined, NH_4Cl-treated Fe_2O_3 in the presence of H_2O seems to result from a unique interaction of Fe, O, H_2O, Cl, and NO on the surface. Analogies to aqueous coordination chemistry confirm this notion. Both Fe^{2+} and Fe^{3+} display complex and variable coordination stoichiometry and geometry in the presence of aqueous Cl, with pH and Cl concentration exerting large effects.[45,46] Many of these effects have no analogue for salts of other halides. NO adds still more complexity; H_2O, OH^-, Cl^-, and NO (or NO^-) can often coexist in the same coordination sphere. The entire range of behavior does not appear to have been mapped out.

The results of the XPS and pH measurements as a function of calcination temperature point to the following picture of the active surface: a highly acidic, chlorine-rich, hydroxylated environment. Calcination at or below 300 °C appears mainly to desorb NH_3, resulting in N depletion relative to Cl in XPS and yielding a highly basic solution in the effluent-treated water together with a highly acidic residue on the oxide surface. Calcination at excessive temperatures removes Cl, however, as shown by XPS. The deactivation temperature between 300 and 325 °C coincides with the decomposition temperature of bulk $FeCl_3$: 315 °C.[47] The surface remains largely unaffected by the presence of SO_2 or CO_2, presumably because the results showed that neither gas adsorbs appreciably.

That adsorption in this system requires photon illumination points to some charge transfer or redox process taking place during adsorption. The XPS suggests where some of this charge transfer takes place. Surfaces before adsorption support Fe that is 90% in the +3 state and 10% in the +2 state. After adsorption, all the Fe converts to +3. Partial desorption to about 160 °C restores the original Fe^{2+}. TPD[26] shows that completely reversible adsorption of NO can occur only when the surface temperature remains below about 160 °C. Above this temperature, spectral shape depends on the history of surface heating. It seems clear that the "reversible" NO desorbing below 160 °C corresponds to adsorption on the Fe^{2+} sites. An abnormally

low preexponential factor for desorption argues for possible ionization of the NO to the -1 state.[26] Thus, NO adsorbs and ionizes by photoassistance into the -1 state, while the corresponding Fe oxidizes from $+2$ to $+3$.

However, the saturation density of NO roughly equals the density of surface Fe atoms, while only 10% of the Fe seems to change oxidation state. Thus, Fe^{3+} must play a direct role in adsorption, and we cannot ascribe all charge-transfer induced by illumination to Fe^{2+} oxidation alone. Indeed, as we mentioned earlier, several studies of O_2 photoadsorption on metal oxides have suggested (though not proven) that the molecule converts to O_2^- upon adsorption. Perhaps something similar happens to NO. Presumably the excess positive charge from this conversion is accommodated in the space charge region under the semiconductor surface.

Conclusion

Photocatalysis on semiconducting metal oxides remains incompletely understood in many respects. With a view toward deconstructing this complex process, we have examined and manipulated the kinetic characteristics of one component step: photoadsorption. We improved upon the current techniques for extracting adsorption kinetics of illuminated powdered materials. We significantly increased the activity of Fe_2O_3 for NO photoadsorption by treatment with an aqueous NH_4Cl followed by calcination. In doing so, we determined an optimal calcination temperature and probed the chemistry underlying the activation. Unfortunately, the increased activity observed in this system may be unique to a substrate containing $Fe/Cl/H_2O$, and may be sensitive to pretreatment. However, the new experimental methods and explanation for adsorption characteristics on semiconductors should generalize quite readily.

References and Notes

(1) Pruden, A. L.; Ollis, D. F. *J. Catal.* **1983**, *82*, 404.

(2) Hidaka, H.; Kubota, H.; Gratzel, M.; Pelizzetti, E.; Serpone, N. *J. Photochem.* **1986**, *35*, 219.

(3) Pelizzetti, E.; Minero, C.; Pramauro, E.; Barbeni, M.; Maurino, V.; Tosato, M. *Chim. Ind.* **1987**, *69*, 88.

(4) Krautler, B.; Bard, A. J.; *J. Am. Chem. Soc.* **1978**, *100*, 4317.

(5) Barbeni, M.; Pramauro, E.; Pelizzetti, E.; Borgarello, E.; Serpone, N. *Chemosphere* **1985**, *14*, 195.

(6) Munuera, G.; Rives-Arnau, V.; Saucedo, A. *J. Chem. Soc., Faraday Trans. I* **1979**, *75*, 736.

(7) Courbon, H.; Herrmann, J. M.; Pichat, P. *J. Phys. Chem.* **1984**, *88*, 5210.

(8) Bickley, R. I.; Stone, F. S. *J. Catal.* **1973**, *31*, 389.

(9) Ditchfield, R.; Llera-Rodríguez, D.; Seebauer, E. G. *Phys. Rev. Lett.* **1998**, *81*, 1259.

(10) Baidyaroy, S.; Bottoms, W. R.; Mark, P. *Surf. Sci.* **1971**, *28*, 517.

(11) Genequand, P. *Surface Sci.* **1971**, *25*, 643.

(12) Ibusuki, T.; Takeuchi, K. *J. Mol. Catal.* **1994**, *88*, 93.

(13) Pichat, P.; Herrmann, J. M.; Courbon, H.; Disdier, J.; Mozzanega, M. N. *The Can. J. Chem. Eng.* **1982**, *60*, 27.

(14) Hori, Y.; Fujimoto, K.; Suzuki, S. *Chem. Lett.* **1986**, *11*, 1845.

(15) Kase, K.; Yamaguchi, M.; Suzuki, T.; Kaneko, K. *J. Phys. Chem.* **1995**, *99*, 13307.

(16) Malati, M. A.; Wong, W. K. *Surf. Technol.* **1984**, *22*, 305.

(17) Martin, S. T.; Morrison, C. L.; Hoffmann, M. R. *J. Phys. Chem.* **1994**, *98*, 13695.

(18) Criado, J. J.; Macias, B.; Rives, V. *React. Kin. Catal. Lett.* **1985**, *27*, 313.

(19) Matsumoto, Y.; Kurimoto, J.; Amagasaki, Y.; Sato, E. *J. Electrochem. Soc.* **1980**, *127*, 2148.

(20) Martin, S. T.; Herrmann, H.; Hoffmann, M. R. *J. Chem. Soc., Faraday Trans.* **1994**, *90*, 3323.

(21) Choi, W.; Termin, A.; Hoffmann, M. R.; *J. Phys. Chem.* **1994**, *98*, 13669.

(22) Gonzalez-Elipe, A. R.; Munuera, G.; Sanz, J.; Soria, J. *J. Chem. Soc. Faraday Trans. I* **1980**, *76*, 1535.

(23) Boonstra, A. H.; Mutsaers, C. A. H. A. *J. Phys. Chem.* **1975**, *79*, 1694.

(24) Gonzalez-Elipe, A. R.; Munuera, G.; J.; Soria, J. *J. Chem. Soc. Faraday Trans. I* **1979**, *75*, 1748.

(25) Bickley, R. I.; Jayanty, R. K. M. *Discuss. Faraday Soc.* **1974**, *58*, 194.

(26) Blomiley, E. R.; Seebauer, E. G., *Langmuir* 1999. In press.

(27) Strehlow, W. H.; Cook, E. L. *J. Phys. Chem. Ref. Data* **1973**, *2*, 163.

(28) Tinnemans, A. H. A.; Koster, T. P. M.; Thewissen, D. H. M. W.; Mackor, A. *Ber. Bunsen-Ges. Phys. Chem.* **1986**, *90*, 383.

(29) Grätzel, M.; Kiwi, J.; Morrison, C. L. *J. Chem. Soc. Faraday Trans. I* **1985**, *81*, 1883.

(30) King, D. A.; Wells, M. G. *Surf. Sci.* **1972**, *29*, 454.

(31) Israelachvili, J. *Intermol. Surf. Forces*, 2nd ed.; Academic Press: San Diego, 1992; Chapter 7.

(32) In $P(t)$ data, such as those of Figure 7, the effects of the three parameters in S remain well-decoupled in the fitting procedure. N_{sat} primarily determines how quickly P_o is recovered, m determines the curvature of the plot after the minimum is reached, and S_o determines the depth of the minimum.

(33) Bartholomew, C. H.; Agrawal, P. K.; Katzer, J. R. *Adv. Catal.* 1981, *31*, 135.

(34) Czarnecki J.; Pereira, M.; Zak, K. P. *Pollut. Eng.* **1994**, *26*, 26.

(35) Hoffmann, A. J.; Yee, H.; Mills. G.; Hoffmann, M. R. *J. Phys. Chem.* **1992**, *96*, 5540.

(36) Wei, T. Y.; Wan, C. C. *Ind. Eng. Chem. Res.* **1991**, *30*, 1293.

(37) Al-Sayyed, G.; D'Oliveira, J. C.; Pichat, P. *J. Photochem. Photobiol. A: Chem.* **1991**, *58*, 99.

(38) Serpone, N., Pelizzetti, E., Eds. *Photocatalysis Fundamentals and Applications*; Wiley-Interscience: New York, 1989; p 135.

(39) Hoffmann, M. R.; Martin, S. T.; Choi, W.; Bahnemann, D. W. *Chem. Rev.* **1995**, *95*, 69.

(40) TPD also revealed a small amount (5%) of NO_2 desorption.

(41) This observation is true at least in the range of rates considered here.

(42) Peral, J.; Ollis, D. F. *J. Catal.* **1992**, *136*, 554.

(43) Idriss, H.; Miller, A.; Seebauer, E. G. *Catal. Today* **1997**, *33*, 215.

(44) Morrison, S. R. *The Chemical Physics of Surfaces*, 1st ed.; Plenum Press: New York, 1977; Chapter 9.

(45) Brady, G. W.; Robin, M. B.; Varimbi, J. *Inorg. Chem.* **1964**, *3*, 1168.

(46) Nicholls, D. *Comprehensive Inorganic Chemistry*, 1st ed.; Pergamon Press Ltd.: Oxford, 1973; Vol. 3, Chapter 40.

(47) *CRC Handbook of Chemistry Physics*, 79th ed.; Chemical Rubber Publishing Company: Boca Raton, 1998; Section 4.